Published in International Journal of Quantum Chemistry 102: 119-131, 2005

Calculation of Spin-Orbit Coupling Within the LFDFT: Applications to $[NiX_4]^{2-}$ (X=F$^-$, Cl$^-$, Br$^-$, I$^-$)

MIHAIL ATANASOV,[2] CÉDRICK RAUZY,[1] PIO BAETTIG,[1] CLAUDE DAUL[1]

[1]*Département de Chimie, Université de Fribourg, Chemin du Musée, 9, CH-1700 Fribourg, Switzerland*

[2]*Institute of General and Inorganic Chemistry, Bulgarian Academy of Sciences Acad. G. Bontchev Str. Bl. 11, 1113 Sofia, Bulgaria*

Received 5 April 2004; accepted 28 June 2004
Published online 6 December 2004 in Wiley InterScience (www.interscience.wiley.com).
DOI 10.1002/qua.20376

ABSTRACT: Spin-orbit coupling has been introduced into our newly developed ligand field density functional theory (LFDFT), using the zero-order regular approximation as implemented into the Amsterdam density functional (ADF) code. Application of the formalism to a series of NiX_4^{2-} (X=F$^-$, Cl$^-$, Br$^-$, I$^-$) compounds shows the increasing importance of intra-ligand spin-orbit coupling across the F, Cl, Br, I series, to lead to sign reversal (in the case of Br$^-$ and I$^-$) of the spin-orbit splitting within the t_2-orbitals manifold of Ni^{2+}. Symmetry lowering from T_d to D_{2d}, due to the Jahn–Teller coupling for the $e^4t_2^4$ configuration of NiX_4^{2-}, is used to manifest further the effect of bonding changes on the sign and magnitude of the spin-orbit constant. Ligand field and spin-orbit coupling matrices are found to be correlated, with the higher erxtent of antibonding being accompanied by lower values of the spin-orbit coupling constant. In cases of little or no symmetry, this leads to situations in which ligand field and spin-orbit coupling cannot be neatly separated in the mathematical description. Using these results, the electronic energy levels of this series of compounds are predicted to be in good agreement with available spectral and magnetic data from literature.

Key words: spin-orbit coupling; density functional theory; ligand field theory; Jahn–Teller effect; zero field splitting

1. Introduction

Spin-orbit coupling is an essential constituent of the Hamiltonian for electronic states originating from d^n-configurations of transition metals in ligand fields (LF). It governs the fine structure of the electronic multiplets and, for the ground state it is mainly responsible for the zero-field splitting and the anisotropy affecting the spectroscopic and magnetic behavior of TM compounds with open *d*-shells. Recently, we proposed a ligand field density functional theory [1, 2] (LFDFT), which is a DFT-based method to determine ligand field parameters. Modern functionals, which are all based

Correspondence to: C. Rauzy; e-mail: cedrick.rauzy@unifr.ch
Contract grant sponsor: Swiss National Science Foundation.

on quantum Monte Carlo treatment of a homogeneous electron gas, contain most of the dynamical correlation. The nondynamical or near-degeneracy correlation however is missing. The key feature of our approach is the explicit treatment of near-degeneracy correlation using ad hoc configuration interaction (CI) within the active space of Kohn–Sham (K–S) orbitals with dominant *d*- or *f*-character. The calculation of the CI matrices is based on a symmetry decomposition and/or on a ligand field (LF) analysis of the energies of all single determinants (micro-states) calculated according to density functional theory (DFT) for frozen K–S-orbitals corresponding to the averaged configuration, eventually with fractional occupations, of the *d*- or *f*-orbitals. This procedure yields multiplet energies with an accuracy within 2,000 cm^{-1}. The accuracy of this approximation can be judged from the agreement between calculated and observed transition energy [1, 2]. We extended the domain of application of this formalism to more than one TM. This allowed us [3, 4] to treat exchange coupling and mixed valency on the same footing.

In this contribution, we extend the LFDFT with the inclusion of spin-orbit coupling. A good opportunity to achieve this consist in using the zero-order regular approximation [5] (ZORA), which permits the inclusion of spin-orbit coupling effects variationally. ZORA has been implemented into the Amsterdam density functional (ADF) program [6] and has been proved to work well.

This contribution is organized as follows. Section 2 describes spin-orbit coupling in T_d symmetry and in its subgroup D_{2d}. Section 3 presents the implementation of the formalism along the lines of LFDFT. Thus, it is possible to obtain symmetry consistent spin-orbit coupling parameters without recourse to the implicit use of orbital reduction factors. We intend to show that orbital dependence of that kind can be larger than one might expect. We will show that it is possible to apply the formalism, using data from DFT-ZORA calculations. Finally, we apply the theory to the NiX_4^{2-} (X=F$^-$, Cl$^-$, Br$^-$, I$^-$) series of compounds and compare the results with experimental data from the literature. An outlook toward an extension of the theory to systems with little or no symmetry will also be given.

2. Spin-Orbit Coupling

Spin-orbit coupling cannot be ignored when ions or molecules contain heavy elements. The effect is not very large for first-row elements and is more pronounced in their magnetic properties. However, for second- and third-row transition metals, as well as for the *f*-elements, even qualitative accounts of electronic absorption spectra cannot neglect spin-orbit effects. Similarly, for molecular orbitals calculations in which ligands play an important role, spin-orbit coupling due to ligands, e.g., iodide or bromide, must be considered.

2.1. THEORETICAL DESCRIPTION

The nature and origin of spin–orbit coupling have been discussed by many investigators [7]. Misetich and Buch [8] have shown that the spin-orbit Hamiltonian of a molecule can be approximated reasonably well as

$$\hat{H}_{SO} = \sum_{N,i} \zeta_N \cdot \vec{l}_{i,N} \cdot \vec{s}_i = \sum_i \vec{u}_{i,N} \cdot \vec{s}_i, \qquad (1)$$

where ζ_N, the spin-orbit coupling constant of nucleus N, is incorporated into the molecular operator $\vec{u}_i$ for electron i.

To carry out a spin-orbit calculation, it is necessary to relate the resultant splitting of many electron states and also the interaction of different states to one-electron spin-orbit coupling matrix elements. This can be done most conveniently on the basis of micro-states (single determinants), as shown in Refs. [1, 2, 9] for the calculation of multiplets, using Slater's rules. Indeed, the calculation of matrix elements of one- and two-electron operators between determinantal N-electron wave functions is straightforward. For the spin-orbit interaction, only one-electron operators are involved. Calculation of the corresponding matrix elements is described next.

The spin-orbit operator in Eq. (1) enables the expression of matrix elements of spin-orbit coupling in and between subshells in terms of molecular orbitals. Thus, any arbitrary one-electron spin-orbit coupling matrix element can be written as:

$$\begin{aligned}\langle sm_s, a\alpha|\hat{H}_{SO}|sm'_s, b\beta\rangle &= \langle sm_s, a\alpha|\vec{u}\cdot\vec{s}|sm'_s, b\beta\rangle \\ &= \sum_{k=x,y,z} \langle sm_s|s_k|sm'_s\rangle \\ &\quad \times \langle a\alpha|u_k|b\beta\rangle, \qquad (2)\end{aligned}$$

where s is the spin of a single electron with component m_s; a and b are the irreducible representa-

tions (irrep.) of the molecular orbitals; and α and β are the corresponding components in the case of degeneracy. The first term on the right-hand side of Eq. (2) is no more than the Pauli matrices and the second term can be further reduced using Wigner–Eckhardt's theorem:

$$\langle a\alpha|u_k|b\beta\rangle = \langle a\alpha|b\beta,\, t_1k\rangle\langle a\|u\|b\rangle, \tag{3}$$

where $\langle a\alpha|b\beta,\, t_1k\rangle$ are coupling coefficients for the tetrahedral group and $\langle a\|u\|b\rangle$ are reduced matrix elements. Combining Eqs. (2) and (3) enables us to express any arbitrary spin-orbit matrix element as a product of symmetry coefficients and reduced matrix elements:

$$\langle sm_s,\, a\alpha|\hat{H}_{SO}|sm_s',\, b\beta\rangle = \langle a\|u\|b\rangle \sum_{k=x,y,z} \langle s,\, m_s|\hat{s}_k|sm_s'\rangle \times \langle a\alpha|b\beta,\, t_1k\rangle. \tag{4}$$

To estimate the still unknown reduced spin-orbit coupling matrix elements $\langle a\|u\|b\rangle$, we shall map Eq. (4) onto a ZORA-DFT calculation and adjust the reduced matrix elements to reproduce the calculated ligand field levels as done previously in LF-DFT. This task requires a symmetry adaptation of the K–S molecular orbitals to the double-group T_d^*, i.e.,

$e \otimes \Gamma_6(\alpha,\, \beta) = \Gamma_8$:

$$|\Gamma_8(e) : \kappa\rangle = -|e\varepsilon,\, \beta\rangle;$$
$$|\Gamma_8(e) : \lambda\rangle = |e\theta,\, \alpha\rangle;$$
$$|\Gamma_8(e) : \mu\rangle = -|e\theta,\, \beta\rangle;$$
$$|\Gamma_8(e) : \nu\rangle = |e\varepsilon,\, \alpha\rangle;$$

$t_2 \otimes \Gamma_6(\alpha,\, \beta) = \Gamma_8$:

$$|\Gamma_8(t_2) : \kappa\rangle = \frac{1}{\sqrt{6}}|t_2\xi,\, \alpha\rangle - \frac{i}{\sqrt{6}}|t_2\eta,\, \alpha\rangle + \frac{2}{\sqrt{6}}|t_2\zeta,\, \beta\rangle;$$

$$|\Gamma_8(t_2) : \lambda\rangle = -\frac{1}{\sqrt{2}}|t_2\xi,\, \beta\rangle + \frac{i}{\sqrt{2}}|t_2\eta,\, \beta\rangle;$$

$$|\Gamma_8(t_2) : \mu\rangle = \frac{1}{\sqrt{2}}|t_2\xi,\, \alpha\rangle + \frac{i}{\sqrt{2}}|t_2\eta,\, \alpha\rangle;$$

$$|\Gamma_8(t_2) : \nu\rangle = -\frac{1}{\sqrt{6}}|t_2\xi,\, \beta\rangle - \frac{i}{\sqrt{6}}|t_2\eta,\, \beta\rangle + \frac{2}{\sqrt{6}}|t_2\zeta,\, \alpha\rangle$$

$t_2 \otimes \Gamma_6(\alpha,\, \beta) = \Gamma_7$:

$$|\Gamma_7(t_2) : \alpha''\rangle = \frac{1}{\sqrt{3}}|t_2\xi,\, \beta\rangle + \frac{i}{\sqrt{3}}|t_2\eta,\, \beta\rangle + \frac{1}{\sqrt{3}}|t_2\zeta,\, \alpha\rangle;$$

$$|\Gamma_7(t_2) : \beta''\rangle = \frac{1}{\sqrt{3}}|t_2\xi,\, \alpha\rangle - \frac{i}{\sqrt{3}}|t_2\eta,\, \alpha\rangle - \frac{1}{\sqrt{3}}|t_2\zeta,\, \beta\rangle, \tag{5}$$

where the notation of the double-group representation is according to Bethe, and their components are Griffith's [10]. Using this basis transformation along with spin-orbit coupling elements (Appendix 1), the one-electron spin-orbit coupling and LF matrix reduces to:

	$\Gamma_8(e)$	$\Gamma_8(t_2)$	$\Gamma_7(t_2)$
$\Gamma_8(e)$	h_{ee}	$-\sqrt{\frac{3}{2}}\, i\zeta_{et_2}^{t_1}$	0
$\Gamma_8(t_2)$	$\sqrt{\frac{3}{2}}\, i\zeta_{et_2}^{t_1}$	$h_{t_2t_2} - \frac{1}{2}\zeta_{t_2t_2}^{t_1}$	0
$\Gamma_7(t_2)$	0	0	$h_{t_2t_2} + \zeta_{t_2t_2}^{t_1}$,

(6)

where h_{ee} and $h_{t_2t_2}$ are the one-electron ligand field matrix elements, the $h_{t_2t_2}$–h_{ee} difference being the cubic field splitting Δ, and $\zeta_{et_2}^{t_1}$ and $\zeta_{t_2t_2}^{t_1}$ the reduced matrix elements:

$$\zeta_{et_2}^{t_1} = \langle e\|\vec{s}\vec{u}(t_1)\|t_2\rangle$$
$$\zeta_{t_2t_2}^{t_1} = \langle t_2\|\vec{s}\vec{u}(t_1)\|t_2\rangle, \tag{7}$$

which we derive in a form to be directly compared with the free Ni^{2+} spin-orbit coupling constant (630 cm^{-1}). Section 3.3 describes a procedure of obtaining these parameters from ZORA-DFT calculations.

The $^3T_1$ ground state of Ni^{2+} (d^8) in a tetrahedral (T_d) ligand field is Jahn–Teller unstable and distorts toward tetragonal D_{2d} symmetry with elongation along the S_4 axis of the tetrahedron. For this point group, the symmetry species $t_2(\xi,\, \eta,\, \zeta)$ and $e(\theta,\, \varepsilon)$ split into $e(\xi,\, \eta) + b_2(\zeta)$ and $a_1(\theta) + b_1(\varepsilon)$, respec-

tively. Symmetry adaptation of the K–S molecular orbitals to the D_{2d}^* double group yields
$a_1 \otimes \Gamma_6(\alpha, \beta) = \Gamma_6$:

$$|\Gamma_6(a_1), \alpha'\rangle = |a_1\theta, \alpha\rangle$$
$$|\Gamma_6(a_1), \beta'\rangle = |a_1\theta, \beta\rangle$$

$e \otimes \Gamma_6(\alpha, \beta) = \Gamma_6$:

$$|\Gamma_6(e), \alpha'\rangle = \frac{1}{\sqrt{2}}|e\xi, \beta\rangle - \frac{i}{\sqrt{2}}|e\eta, \beta\rangle$$
$$|\Gamma_6(e), \beta'\rangle = \frac{1}{\sqrt{2}}|e\xi, \alpha\rangle + \frac{i}{\sqrt{2}}|e\eta, \alpha\rangle$$

$b_1 \otimes \Gamma_6(\alpha, \beta) = \Gamma_7$:

$$|\Gamma_7(b_1), \alpha''\rangle = -|b_1\varepsilon, \beta\rangle$$
$$|\Gamma_7(b_1), \beta''\rangle = |b_1\varepsilon, \alpha\rangle$$

$b_2 \otimes \Gamma_6(\alpha, \beta) = \Gamma_7$:

$$|\Gamma_7(b_2), \alpha''\rangle = |b_2\zeta, \beta\rangle$$
$$|\Gamma_7(b_2), \beta''\rangle = |b_2\zeta, \alpha\rangle$$

$e \otimes \Gamma_6(\alpha, \beta) = \Gamma_7$:

$$|\Gamma_7(e), \alpha''\rangle = \frac{1}{\sqrt{2}}|e\xi, \alpha\rangle - \frac{i}{\sqrt{2}}|e\eta, \alpha\rangle$$
$$|\Gamma_7(e), \beta''\rangle = -\frac{1}{\sqrt{2}}|e\xi, \beta\rangle + \frac{i}{\sqrt{2}}|e\eta, \beta\rangle, \qquad (8)$$

where again double-group representations are according to Bethe. Using this basis transformation along with the spin-orbit coupling matrix elements (Appendix 1), we obtain the spin-orbit coupling and LF matrix for this symmetry

	$\Gamma_6(a_1)$	$\Gamma_6(e)$	$\Gamma_7(b_1)$	$\Gamma_7(b_2)$	$\Gamma_7(e)$
$\Gamma_6(a_1)$	$h_{a_1a_1}$	$\sqrt{\frac{3}{2}}\, i\zeta^{e}_{a_1e}$	0	0	0
$\Gamma_6(e)$	$-\sqrt{\frac{3}{2}}\, i\zeta^{e}_{a_1e}$	$h_{ee} - \frac{1}{2}\zeta^{a_2}_{ee}$	0	0	0
$\Gamma_7(b_1)$	0	0	$h_{b_1b_1}$	$-i\zeta^{a_2}_{b_1b_2}$	$\frac{-i}{\sqrt{2}}\zeta^{e}_{b_1e}$
$\Gamma_7(b_2)$	0	0	$i\zeta^{a_2}_{b_1b_2}$	$h_{b_2b_2}$	$\frac{-1}{\sqrt{2}}\zeta^{e}_{b_2e}$
$\Gamma_7(e)$	0	0	$\frac{i}{\sqrt{2}}\zeta^{e}_{b_1e}$	$\frac{-1}{\sqrt{2}}\zeta^{e}_{b_2e}$	$h_{ee} + \frac{1}{2}\zeta^{a_2}_{ee}$,

(9)

where $h_{a_1a_1}$, h_{ee}, $h_{b_1b_1}$, $h_{b_2b_2}$ are the (diagonal in this case as well) one-electron ligand field matrix elements and ζ^{k}_{ij} are the reduced matrix elements:

$$\zeta^{e}_{a_1e} = \langle a_1\|\vec{s}\vec{u}(e)\|e\rangle$$
$$\zeta^{a_2}_{b_1b_2} = \langle b_1\|\vec{s}\vec{u}(a_2)\|b_2\rangle$$
$$\zeta^{e}_{b_1e} = \langle b_1\|\vec{s}\vec{u}(e)\|e\rangle$$
$$\zeta^{a_2}_{ee} = \langle e\|\vec{s}\vec{u}(a_2)\|e\rangle$$
$$\zeta^{e}_{b_2e} = \langle b_2\|\vec{s}\vec{u}(e)\|e\rangle. \qquad (10)$$

We note that in D_{2d}^* symmetry, the cubic quantities $\zeta^{t_1}_{et_2}$ and $\zeta^{t_1}_{t_2t_2}$ split into three and two different reduced matrix elements, respectively, yielding a total of five independent parameters. In LF studies, thus far the variation of spin-orbit coupling between the various symmetries of the involved LF-orbitals have been approximated in terms of orbital reduction factors. In the next section, we derive a rigorous procedure that allows us to deduce these quantities from DFT-ZORA calculations.

3. Computational Procedure

The DFT calculations have been performed with the aid of the ADF program code (release 2003.01) [6]. For the exchange-correlation functionals, both

the local density approximation (LDA, for geometry optimizations) and the generalized gradient approximation (GGA) (for energies of electronic states) have been used. For LDA, we adopt an Xα functional for exchange ($\alpha = 0.7$) [11] and Vosko, Wilk, and Nusair functional for correlation [12]. The GGA has been introduced in the form given by Perdew–Wang [13]. The frozen-core approximation was used for inner core electrons. The orbitals up to 3*p* for Ni, 1*s* for fluorine, 2*p* for chlorine, 3*d* for bromine, and up to 4*d* for iodine were kept frozen. The valence shells were described by triple zeta plus one polarization function (TZP basis set). Spin-restricted relativistic ZORA calculations have been done by adopting the ZORA basis set (TZP) [14]. Using basis functions of icnreasing quality from TZP to TZ2P to TZ2P+ does not change results significantly (see Section 4.4).

3.1. GEOMETRY OPTIMIZATIONS

Geometry optimizations of the NiX_4^{2-} species have been done in nonrelativistic spin-unrestricted ($M_s = 1$) formalism, using the LDA-only functional, which we know from experience [2] to yield TM–ligand bond distances in good agreement with experiment. To study the Jahn–Teller activity within the $^3T_1$ ground state, separate optimizations imposing a D_{2d} geometry have been carried out following the guidelines of accounting for the Jahn–Teller effect within DFT [15]. It should be noted that, as a single determinant method, DFT is unable to yield optimized geometries in the case in which two or more configurations mix with each other. This is the case in our study, where two $^3A_2$ states (originating from $^3T_1$ in tetrahedral symmetry), corresponding to the ground configuration ($e^4t_2^4$) and to the excited configuration ($e^3t_2^5$), mix and reduce the extent of the structural distortion and of the Jahn–Teller stabilization (E_{JT}) [16]. A procedure to solve this problem is briefly outlined in Appendix 2 and is used here to obtain ground-state D_{2d} geometries for all NiX_4^{2-} species.

3.2. LFDFT CALCULATIONS

The LFDFT method is well documented [1, 2]. In short, the following steps are considered. Having chosen a reference geometry (see Section 3.1), an average of configuration spin-restricted (AOC) calculation is performed with eight electrons distributed evenly over the five 3*d*-molecular orbitals. The latter are identified as such, according to their dominant metal character, inspecting the K–S eigenvectors. Constraining the electron density to this distribution of charge, the energies of all 45 Slater determinants are calculated in a spin-unrestricted way. Using the two 5×5 matrices of K–S 3*d*-eigenvalues (diagonal matrix) and their MO coefficients along with the energies of the SD our formalism (implemented into a MATLAB script) yields the parameters of interelectronic repulsion *B* and *C* and the 5×5 LF matrix, which in our case takes a diagonal form with two different energies (*e* and t_2) for T_d and four different energies ($h_{a_1a_1}$, $h_{b_1b_1}$, $h_{b_2b_2}$, and h_{ee}) for D_{2d}. (MATLAB 6.1 scripts and programs written for each system can be obtained from the authors on request.) At the same time, the program yields the energies of all 45 electronic states in an LF multiplet calculation. This corresponds to a CI procedure within the DFT formalism.

3.3. CALCULATION OF REDUCED MATRIX ELEMENTS OF SPIN-ORBIT COUPLING FROM ZORA-DFT

Let us consider the K–S eigenvalues in the basis of the double group symmetry adapted fragment orbitals (SFO) and the symmetry adapted fragment spin-orbitals [see Eqs. (5) and (8)]. To be more specific let us take as an example $NiCl_4^{2-}$. Focusing on the T_d complex, the $5t_1$, $16t_2$, and 8*e* spin-orbitals give rise to a total of $29\Gamma_8$ and $16\Gamma_7$ K–S-orbitals, from which we identify the $6\Gamma_8$, $7\Gamma_8$, and $4\Gamma_7$ ones with dominant 3*d* character. We correspondingly occupy these evenly in the ZORA input with occupation numbers and ZORA eigenvalues taken from the output listed in Eq. (11). We further find from the table of the SFO, 8, 5, and 16 species of *E*, T_1, and T_2 symmetry, yielding a total of 29 basis functions for Γ_8 and 16 T_2 species, giving rise to the same number of Γ_7 species. These yield the coefficients of the $6\Gamma_8$, $7\Gamma_8$, and $4\Gamma_7$ K–S-ZORA eigenvectors. We thus obtain truncated ZORA-K–S eigenvectors and (diagonal) eigenvalues matrices **U** and Λ [Eqs. (11)]:

$$U = \begin{array}{c} \\ e \\ t_2 \\ t_2 \end{array} \begin{array}{c} \begin{array}{ccc} 6\Gamma_8 & 7\Gamma_8 & 4\Gamma_7 \end{array} \\ \begin{bmatrix} -0.842 & -0.135 & 0.0 \\ -0.104 & 0.789 & 0.0 \\ 0.0 & 0.0 & -0.816 \end{bmatrix} \end{array}$$

$$\Lambda = \begin{array}{c} \\ 6\Gamma_8 \\ 7\Gamma_8 \\ 4\Gamma_7 \end{array} \begin{array}{c} \begin{array}{ccc} 6\Gamma_8 & 7\Gamma_8 & 4\Gamma_7 \end{array} \\ \begin{bmatrix} 2.940 & 0.0 & 0.0 \\ 0.0 & 3.458 & 0.0 \\ 0.0 & 0.0 & 3.509 \end{bmatrix} \end{array} \quad (11)$$

$$S = U \cdot U^T \quad (12)$$

TABLE I

Bond lengths (in Å), the extent of Jahn–Teller elongation of the tetrahedral into the D_{2d} ground-state energy minima ($\delta\theta_{min}$ in °) and the Jahn–Teller stabilization energy E_{JT} (in cm^{-1}) for NiX_4^{2-} (X=F^-, Cl^-, Br^-, and I^-).*

X	R	$\delta\theta_{min}$	E_{JT}
F	1.94	−5.2 [−8.3]	−335 [−825]
Cl	2.29	−3.1 [−5.5]	−83 [−260]
Br	2.44	−2.9 [−5.3]	−62 [−198]
I	2.64	0.0 [−4.6]	0 [−49]

* Spin-unrestricted DFT geometry optimizations (VWN-LDA functional) with and without (in square brackets) taking mixing between $^3T_1(e^4t_2^4)$ and $^3T_1(e^3t_2^5)$ into account (still described by single determinants) have been performed, using a strategy described in Appendix 2.

$$h = \{h_{\mu\nu}\} = S^{-(1/2)}U\Lambda U^T S^{(-1/2)} \tag{13}$$

$$h = \begin{array}{c} \\ e(\Gamma_8) \\ t_2(\Gamma_8) \\ t_2(\Gamma_7) \end{array} \begin{array}{c} \begin{array}{ccc} e(\Gamma_8) & t_2(\Gamma_8) & t_2(\Gamma_7) \end{array} \\ \begin{bmatrix} 2.951 & -0.074i & 0.0 \\ 0.074i & 3.447 & 0.0 \\ 0.0 & 0.0 & 3.509 \end{bmatrix} \end{array}. \tag{14}$$

After manipulations as described in Eqs. (12) and (13), we obtain the one-electron Hamiltonian matrix [Eq. (14)]. The comparison with Eq. (6) yields directly the reduced matrix elements $\zeta^{t_1}_{t_2t_2}$ and $\zeta^{t_1}_{et_2}$, as well as the cubic ligand splitting Δ (333, 487, and 4,166 cm^{-1}, respectively). In a similar way, the matrices of the spin-orbit coupling plus the LF for $NiCl_4^{2-}$ in D_{2d} symmetry are derived from matrix 15. Using definition Eq. (10), this yields the LF and

$$\begin{array}{c} \\ \Gamma_6(a_1) \\ \Gamma_6(e) \\ \Gamma_7(b_1) \\ \Gamma_7(b_2) \\ \Gamma_7(e) \end{array} \begin{bmatrix} 2.991 & 0.072i & 0.0 & 0.0 & 0.0 \\ -0.072i & 3.582 & 0.0 & 0.0 & 0.0 \\ 0.0 & 0.0 & 2.950 & -0.063i & -0.040i \\ 0.0 & 0.0 & 0.063i & 3.301 & -0.029 \\ 0.0 & 0.0 & 0.040i & -0.029 & 3.623 \end{bmatrix} \tag{15}$$

spin-orbit coupling matrix elements listed in Table II. Thus, from a single ZORA calculation, both the ligand field and spin-orbit coupling matrices are obtained. To facilitate the analysis of the ADF output, a series of MATLAB scripts are used as interfaces.

4. Applications, Results, and Discussion

4.1. JAHN–TELLER EFFECT AND THE GEOMETRIES OF NiX_4^{2-} (X=F^-, CL^-, BR^-, I^-)

NiX_4^{2-} (X=Cl^-, Br^-, and I^-) are well studied structurally [17, 18] and/or spectroscopically [19–22] and found to exist as slightly distorted ($NiCl_4$) or almost regular tetrahedra ($NiBr_4$ and NiI_4). NiF_4^{2-} remains unknown, Ni^{2+}–F^- complexes tending invariably to adopt a regular octahedral geometry. In line with these observations, our geometry optimizations (Table I) show, that the extent of the Jahn–Teller elongation (Fig. 1) and the stabilization energy is strongly reduced due to mixing between the $e^4t_2^4$ and $e^3t_2^5$ configurations (cf. Appendix 2), the latter configuration being Jahn–Teller stabilized by a D_{2d} compression. In this respect, the $e^3t_2^5$ configuration resembles very much the Jahn–Teller activity in Cu^{2+} with a single hole in the t_2-shell, which readily explains the different stereochemistries of these two ions [16]. Table I (square brackets) also lists geometries and E_{JT} values of NiX_4^{2-} neglecting the $^3T_1(e^4t_2^4)$–$^3T_1(e^3t_2^5)$ mixing. It is this geometry, with more pronounced distortions, that we use to explore the effect of symmetry lowering on the anisotropy of spin-orbit coupling. However, in the discussion of electronic transitions and comparison with the experiment, we make use of the correct geometry.

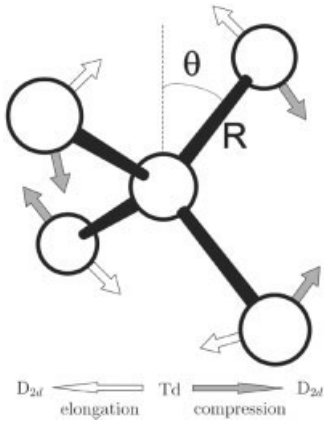

FIGURE 1. Angle θ describing the tetrahedral distortion due to Jahn–Teller activity in NiX_4^{2-}.

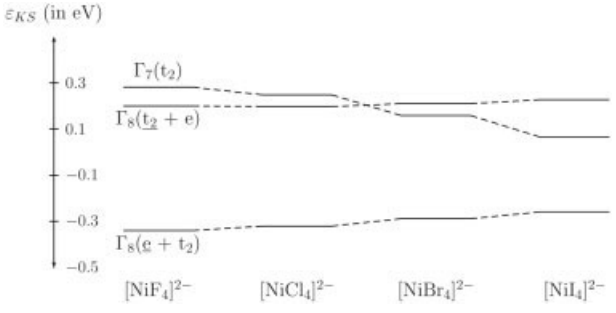

FIGURE 2. Relative energies of Kohn–Sham orbitals with dominant 3*d* character from a ZORA spin-orbit calculation of $[NiX_4]^{2-}$ (X=F$^-$, Cl$^-$, Br$^-$, I$^-$).

4.2. SPIN-ORBIT COUPLING IN T_D SYMMETRY

The (α, β)–e, t_2(3*d*) spin-orbit coupling in T_d symmetry gives rise to $\Gamma_8(e)$ and $\Gamma_8 + \Gamma_7(t_2)$ spinor levels, whose ZORA energies we plot in Figure 2. While spin-orbit coupling leads to splitting of $t_2(\alpha, \beta)$ in first order, it causes a mixing of $\Gamma_8(t_2)$ and $\Gamma_8(e)$ to second order. LF splitting Δ (T_d) is calculated in the range of 4370 (NiF_4^{2-}) to 3395 (NiI_4^{2-}) and dominates over the spin-orbit coupling: $\zeta(Ni^{2+}) = 630$ cm^{-1}; this is accounted for in Figure 2, where dominant contributions from e and t_2 are underlined. We notice that when moving from NiF_4^{2-} to $NiCl_4^{2-}$, the $\Gamma_8(t_2 + e)$–$\Gamma_7(t_2)$ energy separation, which equals (3/2) $\zeta^{t_1}_{t_2t_2}$ [see Eq. (6)], becomes smaller and is lowered further, going to $NiBr_4^{2-}$ and NiI_4^{2-}. It is important to observe that the sign of the splitting changes in the latter two complexes. The analysis of the energy levels (Fig. 2) in terms of the parameters $h_{t_2t_2}$–h_{ee}, $\zeta^{t_1}_{et_2}$ and $\zeta^{t_1}_{t_2t_2}$ [cf. Eq. (6), calculated values are listed in Table II] shows indeed that $\zeta^{t_1}_{t_2t_2}$ becomes negative in the case of $NiBr_4^{2-}$ and NiI_4^{2-}. As has been pointed out previously [22], ligand spin-orbit coupling (as large as 5,000 cm^{-1} for I$^-$!) in combination with the metal (3*d*)–ligand (*np*) mixing can strongly modify the effective spin-orbit couppling constant; this contribution can be of different sign and can even outweigh the spin-orbit coupling due to the 3*d* electrons; this turns the sign of the $\Gamma_8(t_2 + e)$–$\Gamma_7(t_2)$ splitting. Our ZORA calculations lend full support of this proposition, initially observed by MCD data on NiI_4^{2-} [22]. Contrary to earlier interpretations [23], our results indicate that spin-orbit coupling undergoes a stronger decrease with increasing metal–ligand covalency than Stevens's orbital reduction factors in the magnetic moment operator (amenable from a fit to magnetic susceptibilities). Indeed, with increasing covalency from F$^-$ to Cl$^-$ to Br$^-$ to I$^-$, $\zeta^{t_1}_{et_2}$ and $\zeta^{t_1}_{t_2t_2}$ show a much stronger reduction than deduced from orbital reduction factors as the squared MO coefficients c^2_{3d} for 3*d* in the e and t_2 MOs and their combinations [0.82, 0.72, 0.68, 0.66 (e) and 0.75, 0.63, 0.60, 0.56 (t_2) for F$^-$, Cl$^-$, Br$^-$, I$^-$ complexes, respectively]. The order of values for the reduced matrix elements in a given complex $\zeta^{t_1}_{et_2} > \zeta^{t_1}_{t_2t_2}$ (obeyed for all cases in Table I) reflects also subtle changes in the metal–

TABLE II

Ligand field (diagonal) matrix elements and reduced spin-orbit coupling matrix elements for T_d and elongated $T_d \rightarrow D_{2d}$ (in square brackets) DFT optimized (spin-unrestricted, LDA-functional) $[NiX_4]^{2-}$ (X=F$^-$, Cl$^-$, Br$^-$, I$^-$) geometries from ZORA (spin-restricted, LDA + PW91 functional) calculations.

		$[NiF_4]^{2-}$		$[NiCl_4]^{2-}$		$[NiBr_4]^{2-}$		$[NiI_4]^{2-}$	
T_d	$[D_{2d}]$	T_d	$[D_{2d}]$	T_d	$[D_{2d}]$	T_d	$[D_{2d}]$	T_d	$[D_{2d}]$
h_{ee}	$[h_{a_1a_1}(d_{z^2})]$	−2622	[−1904]	−2500	[−2410]	−2277	[−2310]	−2037	[−2150]
	$[h_{b_1b_1}(d_{x^2-y^2})]$		[−3600]		[−2736]		[−2386]		[−2151]
$h_{t_2t_2}$	$[h_{b_2b_2}(d_{xy})]$	1748	[−990]	1667	[95]	1518	[178]	1358	[310]
	$[h_{ee}(d_{xz}, d_{yz})]$		[3247]		[2526]		[2259]		[1945]
$\zeta^{t_1}_{et_2}$	$[\zeta^{e}_{a_1e}]$	588	[576]	488	[474]	373	[337]	375	[222]
	$[\zeta^{e}_{b_1e}]$		[566]		[461]		[300]		[198]
	$[\zeta^{a_2}_{b_1b_2}]$		[598]		[510]		[452]		[410]
$\zeta^{t_1}_{t_2t_2}$	$[\zeta^{a_2}_{ee}]$	518	[516]	332	[326]	−242	[−242]	−832	[−824]
	$[\zeta^{e}_{b_2e}]$		[516]		[329]		[−253]		[−837]

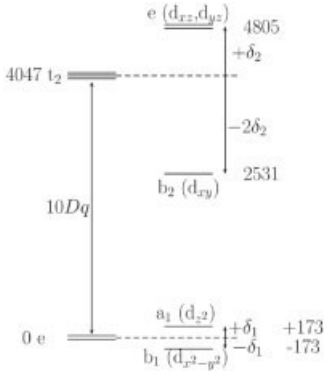

FIGURE 3. Orbital level splittings and notations for a symmetry based description of the D_{2d} distorted (elongated) $NiCl_4^{2-}$ complex for a geometry obtained without correction for $^3T_1(e^4t_2^4)$–$^3T_1(e^3t_2^5)$ missing.

ligand overlap (differential covalency) being larger for the more strongly (σ + π)-antibonding t_2, compared with the only weakly (π)-antibonding e orbital.

4.3. SPIN-ORBIT COUPLING IN D_{2D} SYMMETRY

Going to the D_{2d} distorted T_d complex, the $e(d_{z^2}, d_{x^2-y^2})$ and $t_2(d_{xy}, d_{xz}, d_{yz})$ orbitals split into $a_1(d_{z^2})$ + $b_1(d_{x^2-y^2})$ and $b_2(d_{xy})$ + $e(d_{xz}, d_{yz})$ species and the ligand field matrix becomes fully defined in terms of 10 Dq plus the t_2 and e splitting parameters $3\delta_2$ and $2\delta_1$, respectively. This is illustrated in Figure 3 with parameter values pertaining to $NiCl_4^{2-}$. In parallel with this increase in the level of parameterization, the matrix of spin-orbit coupling becomes dependent on five reduced matrix elements [Eq. (9)]. Figure 5 shows their variation with the angular geometry for $NiCl_4^{2-}$, changing the θ-angle in wide range from elongated to compressed D_{2d} structures. It is striking that the variations of the spin-orbit coupling parameters ζ_{ij}^k follow the same trends as the energies of the correspondingly involved i and j orbitals (Figs. 4 and 5); the stronger the extent of antibonding (increasing the energy of the involved i and j orbitals), the stronger the ζ_{ij}^k reduction. Thus, in an attenuated way, the ζ_{ij}^k parameters reflect the angular dependence of the LF matrix. In classical LF theory, the parameter ζ has been deemed to have an atomic nature, being scaled by some reduction factor, occasionally accounting for axial anisotropy as well. In view of our results, we suggest that such treatments are incomplete. The strong interre-

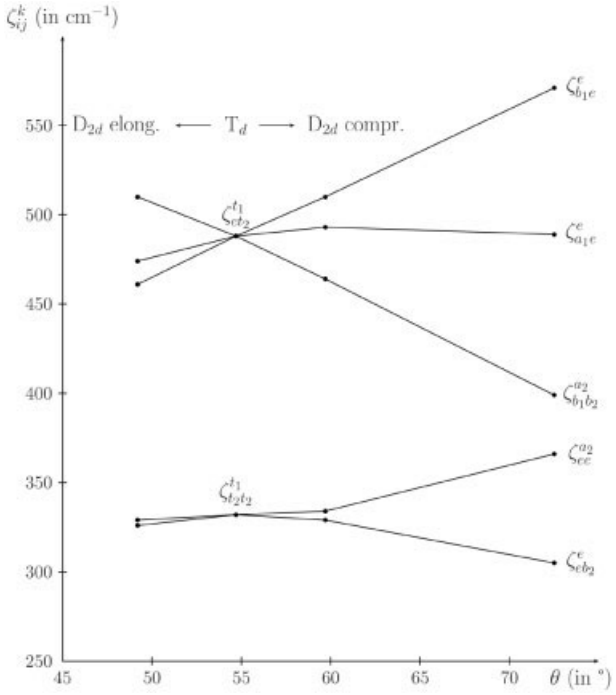

FIGURE 4. Reduced matrix elements of the spin-orbit coupling operator from ZORA-ADF calculations in the T_d and D_{2d} geometries of the $NiCl_4^{2-}$ and their dependence in the geometrical angle θ (see Fig. 1).

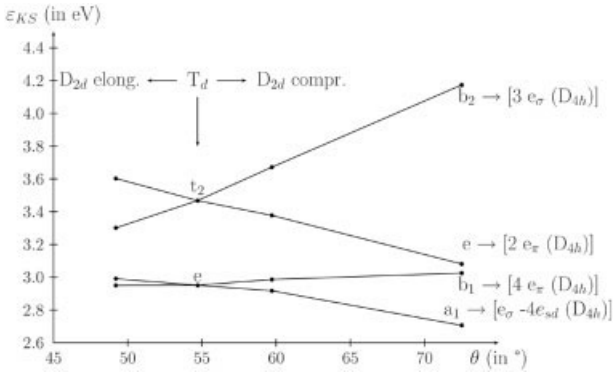

FIGURE 5. Dependence of Kohn–Sham orbital energies from nonrelativistic calculation with average-of-configuration occupancies (T_d: $e^{3.2}t_2^{4.8}$; D_{2d}: $a_1^{1.6}b_1^{1.6}b_2^{1.6}e^{3.2}$) on the geometric angle θ for $NiCl_4^{2-}$ (R = 2.29 Å, PW91-functional, TZP basis). Orbital energy expressions on the right-hand side refer to the limiting case of a compression–square planar geometry and angular overlap model expressions (see Section 4.4).

TABLE III

Ligand field (diagonal) matrix elements and interelectronic repulsion *B* and *C* energies (in cm^{-1}) for T_d and elongated T_d–D_{2d} (in square brackets) DFT-optimized (spin-unrestricted, LDA-functional) $[NiX_4]^{2-}$ (X=F$^-$, Cl$^-$, Br$^-$, I$^-$) geometries from LFDFT (LDA + PW91 functional) calculations.

		$[NiF_4]^{2-}$		$[NiCl_4]^{2-}$		$[NiBr_4]^{2-}$		$[NiI_4]^{2-}$	
T_d	$[D_{2d}]$	T_d	$[D_{2d}]$	T_d	$[D_{2d}]$	T_d	$[D_{2d}]$	T_d	$[D_{2d}]$
h_{ee}	$[h_{a_1a_1}(d_{z^2})]$	−2494	[−1696]	−2428	[−2320]	−2274	[−2321]	−2034	[−2226]
	$[h_{b_1b_1}(d_{x^2-y^2})]$		[−3528]		[−2666]		[−2363]		[−2032]
$h_{t_2t_2}$	$[h_{b_2b_2}(d_{xy})]$	1662	[−999]	1619	[146]	1516	[247]	1356	[445]
	$[h_{ee}(d_{xz}, d_{yz})]$		[3111]		[2420]		[2218]		[1906]
B	[*B*]	715	[713]	521	[521]	462	[458]	401	[399]
C	[*C*]	2732	[2685]	2136	[2126]	1944	[1948]	1804	[1844]

lation between the LF and molecular spin-orbit forces can even invalidate the common opinion of the two physical effects, being opposite to each other [24]. In cases of very low symmetry (causing nonzero off-diagonal elements in the matrix $h_{\mu\nu}$), it can even prevent the separation of the one-electron Hamiltonian, in part due to LF and spin-orbit coupling. Fortunately, this is not the case here ($h_{\mu\nu}$ is fully diagonal) to permit a neat separate analysis of the two effects.

4.4. LIGAND FIELD PARAMETERS, GROUND AND EXCITED STATES ENERGIES OF NiX_4^{2-} (X=Cl$^-$, Br$^-$, I$^-$) AND COMPARISON WITH EXPERIMENTAL DATA

A list of LF parameters, the (diagonal) LF matrix and the *B* and *C* values for NiX_4^{2-} halide complexes in T_d and D_{2d} symmetry, is presented in Table III. There is a good agreement between the LFDFT values of 10 Dq for $NiCl_4^{2-}$ (4,150 cm^{-1}) and the one deduced from a direct fit to the spectrum (3,500 cm^{-1} [19] referred to hereafter as "experimental"). However, values of *B* and *C* are, correspondingly, 64% and 68% off from the experimental ones (810 and 3,150 cm^{-1}, respectively) [19]. This can be traced back to the functionals in use that overestimate 3*d*-electron delocalization. A list of LF parameters dependent on the functionals offered by the ADF code (Table IV) shows a weak sensitivity with respect to this choice. Likewise, use of more sophisticated basis functions, such as a quadruple 3*d* basis for Ni^{2+} (TZ2P+) does not alter the values of ζ [causing an increase in ζ (Table II) by 3–4%]. Excited state energies (Table V) for geometries, corresponding to the T_d and D_{2d} energy minima [in this case taking $^3T_1(e^4t_2^4) \rightarrow {}^3T_1(e^3t_2^5)$ mixing into account] shows good agreement between LFDFT and experimental values for the energies of the transitions $^3T_1 \rightarrow {}^3T_2$ and $^3T_1 \rightarrow {}^3A_2$, while the energies of the spin-forbidden transitions to $^1T_2$, ^1E, and $^1T_2$, $^1T_1$, $^1A_1$, as well as the spin-allowed one to $^3T_1$ are found to be by ~4,000 cm^{-1} and 5,500 cm^{-1} smaller than the experimental ones. This is in accordance with the smaller *B* and *C* values and the stronger dependence of the energies of the mentioned states on *B* and *C*.

TABLE IV

Racah's parameters determined with LFDFT method for $[NiCl_4]^{2-}$, using the exchange and correlation functionals available in ADF2003.01.

Experiment [19]		*B* 810 cm^{-1}	*C* 3,150 cm^{-1}	Δ 3,500 cm^{-1}
GGA	PW91	521 cm^{-1}	2,136 cm^{-1}	4,155 cm^{-1}
	PBE	518 cm^{-1}	2,196 cm^{-1}	4,147 cm^{-1}
	RPBE	535 cm^{-1}	2,218 cm^{-1}	4,106 cm^{-1}
	revPBE	530 cm^{-1}	2,212 cm^{-1}	4,115 cm^{-1}
	BLYP	521 cm^{-1}	1,576 cm^{-1}	4,220 cm^{-1}
	LB94	359 cm^{-1}	1,596 cm^{-1}	3,041 cm^{-1}

It is interesting that LF matrices from a nonrelativistic LFDFT calculation and from ZORA differ from each other. These are compared in Table VI, taking the $b_1 \rightarrow a_1$, $b_1 \rightarrow b_2$, and $b_1 \rightarrow e$ energy differences. It can easily be shown, when taking the angular geometry into account, that these differences can be translated into an angular overlap parameterization to yield values of

TABLE V

Multiplet energies (in kK = 10^3 cm^{-1}) for NiX_4^{2-} (X=Cl$^-$, Br$^-$, I$^-$) complexes from LFDFT calculations (zero spin-orbit coupling) in their T_d and D_{2d}-elongated geometries [from DFT geometry optimizations taking mixing between $^3T_1(e^4t_2^4)$ and $^3T_1(e^3t_2^5)$ into account] in comparison with experimental data from literature.

Electronic state	$NiCl_4^{2-}$		$NiBr_4^{2-}$		NiI_4^{2-}	
$T_d(D_{2d})$	LFDFT	Exp. [21]	LFDFT	Exp. 20]	LFDFT	Exp. [22]
$^3T_1(^3A_2, {}^3E)$	0.0 (0.0, 1.87)		0.0 (0.0, 1.65)		0.0 (0.0, 1.24)	
$^3T_2(^3E, {}^3B_2)$	3.48 (4.20, 6.21)	3.84–4.76	3.28 (3.86, 5.80)		2.93 (3.39, 4.99)	
$^3A_2(^3B_1)$	7.53 (9.03)	6.90	7.06 (8.41)	6.40	6.32 (7.47)	
$^1T_2(^1B_2, {}^1E)$	7.64 (7.67, 9.40)	11.69	6.89 (6.92, 8.44)		6.22 (6.34, 7.46)	
$^1E(^1B_1, {}^1A_1)$	7.99 (7.80, 10.08)	12.22	7.19 (7.03, 9.02)		6.47 (6.44, 7.98)	
$^3T_1(^3E, {}^3A_2)$	10.74 (11.44, 13.57)	~14.70	9.69 (10.32, 12.01)		8.49 (9.09, 10.19)	
$^1T_2(^1E, {}^1B_2)$	12.69 (13.61, 15.10)	18.18	11.50 (12.26, 13.75)	(16.50, 17.44)	10.30 (10.94, 12.22)	
$^1T_1(^1E, {}^1A_2)$	14.01 (14.55, 17.06)	19.48	12.71 (13.23, 15.24)	18.13	11.35 (11.97, 13.28)	(13.60, 14.64)
$^1A_1(^1A_1)$	13.79 (15.49)	—	12.47 (14.03)		11.15 (12.45)	14.08
$^1E(^1B_1, {}^1A_1)$	16.38 (17.78, 18.09)	22.08	14.99 (16.25, 16.42)	19.00	13.43 (14.59, 14.66)	(15.75, 15.62)
$^1A_1(^1A_1)$	30.12 (31.55)	—	27.29 (28.56)		24.58 (25.89)	

the parameters for σ- and π-bonding and for mixing of d_{z^2} and 4s (which, being of the same symmetry, i.e., a_1, in D_{2d} can mix with each other), yielding e_σ, e_π, and e_{sd}, respectively. Remarkably, ZORA results reflect a distinctly larger extent of σ- and π-antibonding and e_{sd}-mixing compared with the nonrelativistic LFDFT result. The effect of sd-mixing has a crucial influence via the Fermi contact terms κ on the hyperfine structure tensor A. This is the topic of a separate study [25]. We also notice that the value of the parameter $\zeta_{t_2t_2}^{t_1}$ for $NiCl_4^{2-}$ we deduce from the ZORA results (332 cm^{-1}, Table II) is found in excellent agreement with the one deduced from a fit to magnetic susceptibility data (380 cm^{-1}) [23]. It is this parameter (in combination with the $^3T_1 \times e$ ground-state Jahn–Teller activity, see Appendix 2), that affects the $^3T_1$ ground-state splitting. These are shown in Figure 6 for NiX_4^{2-} (X=Cl$^-$, Br$^-$, and I$^-$). In accordance with large negative $\zeta_{t_2t_2}^{t_1}$ value for NiI_4^{2-} an inverted zero-field splitting pattern for the ground state is calculated with a T_2 ground state and an E excited state 33 cm^{-1} higher in energy. In $NiBr_4^{2-}$ an intermediate coupling scheme is realized with an E ground state and T_2 next in energy. A D_{2d} distortion leads to an A_1 ground state, as is the case in $NiCl_4^{2-}$; however, it originates from the tetrahedral E,

TABLE VI

Orbital interpretations of ligand field energies from LFDFT and ZORA calculations in terms of the AOM parameterization scheme (e_σ, e_π, e_{sd}) along with values of 10 Dq and the t_2-splitting $3\delta_2$ for tetragonally (D_{2d}) elongated $[NiX_4]^{2-}$ (X=F$^-$, Cl$^-$, Br$^-$, I$^-$).

	$[NiF_4]^{2-}$		$[NiCl_4]^{2-}$		$[NiBr_4]^{2-}$		$[NiI_4]^{2-}$	
	LFDFT	ZORA	LFDFT	ZORA	LFDFT	ZORA	LFDFT	ZORA
$E(b_1 \rightarrow a_1)$	1832	1696	346	326	42	76	−194	10
$E(b_1 \rightarrow b_2)$	2529	2610	2812	2831	2610	2564	2477	2461
$E(b_1 \rightarrow e)$	6639	6847	5086	5262	4581	4645	3938	4096
e_σ	6488	6688	4980	5350	4457	4735	3734	4231
e_π	2612	2690	1594	1857	1379	1622	1012	1397
e_{sd}	2277	2629	3402	4094	3910	4382	4359	4562
10 Dq	4353	4597	4155	4289	3903	3913	3548	3550
$3\delta_2$	4110	4237	2274	2431	1971	2081	1461	1635

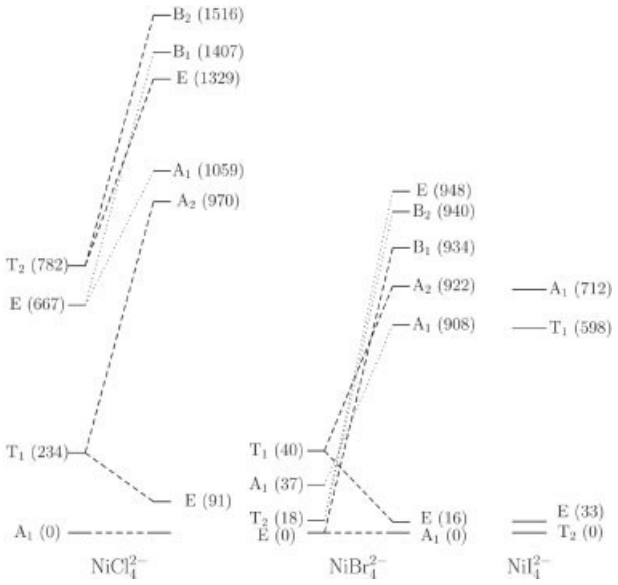

FIGURE 6. Splitting of the $^3T_1$ ground state in T_d geometry due to spin-orbit coupling and in the lower D_{2d} symmetry minimum [for $NiCl_4^{2-}$ and $NiBr_4^{2-}$, $^3T_1(e^4t_2^4)$–$^3T_1(e^3t_2^5)$ mixing is taken into account]. Data for $NiBr_4^{2-}$ are plotted schematically, not following the energy scale for $NiCl_4^{2-}$ and NiI_4^{2-}.

rather than from the tetrahedral A_1, state as in $NiCl_4^{2-}$. It follows that the sign and magnitude of the parameter $\zeta_{t_2t_2}^{t_1}$ is of crucial importance for the ground state splitting. This, as well as the Jahn–Teller activity in the $^3T_1$ ground state, is a further experimental challenge for these systems. For more conclusive results, these compounds should be studied with more modern tools, such as resonance Raman and high-field–high-frequency EPR. We hope this study will motivate further experimental work in this direction.

5. Conclusions

In this work we extended our LFDFT proposed recently [1–4] with spin-orbit coupling, developing a procedure allowing one to extract spin-orbit coupling matrix elements from spin-restricted ZORA calculations. Using symmetry analysis, we show that a set of spin-orbit coupling parameters, rather than a single value or values scaled for anisotropy using (Stevens) orbital reduction factors are needed for a proper description of a realistic situation. In particular, highly covalent ligands such as Br^- and I^- and their own spin-orbit coupling contributions can lead to unexpected, unprecedented splitting patterns of the ground state (zero-field splitting), which deserve further theoretical justification and testing and motivates further experimental work. In subsequent contributions, we will extend the formalism to systems with lower or no symmetry, calculating zero-field splitting for systems well characterized by EPR, thus extending the applicability of our LFDFT approach to fine structure tensor and hyperfine coupling effects.

References

1. Atanasov, M. A.; Daul, C. A.; Rauzy, C. Chem Phys Lett 2003, 367, 737.
2. Atanasov, M. A.; Daul, C. A.; Rauzy, C. Struct Bond 2004, 106, 97.
3. Atanasov, M. A.; Daul, C. A. Chem Phys Lett 2003, 379, 209.
4. Atanasov, M. A.; Daul, C. A. Chem Phys Lett 2003, 381, 584.
5. van Lenthe, E.; Baerends, E. J.; Snijders, J. G. J Chem Phys 1993, 99, 4597.
6. te Velde, G.; Bickelhaupt, F. M.; Baerends, E. J.; Fonseca Guerra, C.; van Gisbergen, S. J. A.; Snijders, J. G.; Ziegler, T. J Comput Chem 2001, 22, 931, and references cited.
7. Slater, J. C. Quantum Theory of Atomic Structure, Vol 2; McGraw-Hill: London, 1960.
8. Misetich, A. A.; Buch, T. J Chem Phys 1964, 41, 2524.
9. Daul, C. A. Int J Quantum Chem 1994, 52, 867.
10. Griffith, J. S. The Theory of Transition Metal Ions; Cambridge University Press: Cambridge, 1961.
11. Slater, J. C. Phys Rev 1951, 81, 385.
12. Vosko, S. H.; Wilk, L.; Nusair, M. Can J Phys 1980, 58, 1200.
13. Perdew, J. P.; Wang, Y. Phys Rev B 1986, 33(12), 8800 corrected 34(E) 7406.
14. ADF Userguide (released 2003.01) http://www.scm.com.
15. Bruyndonckx, R.; Daul, C. A.; Manoharan, P. T.; Deiss, E. Inorg Chem 1997, 36, 4251.
16. Reinen, D.; Atanasov, M.; Nikolov, G. S.; Steffens, F. Inorg Chem 1988, 27, 1678.
17. Pauling, P. Inorg Chem 1966, 5, 1498.
18. Stucky, C. D.; Folkers, J. B.; Kistenmacher, T. J Acta Crystallogr 1967, 23, 1064.
19. Liehr, A. D.; Ballhausen, C. J Ann Phys (NY) 1959, 6, 134.
20. Mooney, A.; Nuttal, R. H.; Smith, W. E. J Chem Soc Dalton Trans 1973, 1920.
21. Koester, V. J.; Dunn, T. M. Inorg Chem 1975, 14, 1811.
22. Collingwood, J. C.; Day, P.; Dennning, R. G. J Chem Soc Faraday II 1973, 591.
23. Gerloch, M.; Slade, R. C. J Chem Soc A 1969, 1012; 1022.
24. Liehr, A. D. J Phys Chem 1960, 64, 43.
25. Atanasov, M.; Baerends, E. J.; Baettig, P.; Bruyndonckx, R.; Daul, C. A.; Rauzy, C.; Zbiri, M. Chem Phys Lett 2004, 399, 433.

Appendix 1: Spin-Orbit Coupling Matrix Elements in T_d and in D_{2d} Symmetry

$\langle a_1[e]\|\vec{s}\vec{u}(e)\|e[t_2]\rangle = \zeta^{e}_{a_1e}$, $\langle b_1[e]\|\vec{s}\vec{u}(e)\|e[t_2]\rangle = \zeta^{e}_{b_1e}$, $\langle b_1[e]\|\vec{s}\vec{u}(a_2)\|b_2[t_2]\rangle = \zeta^{a_2}_{b_1b_2}$, $\langle e[t_2]\|\vec{s}\vec{u}(a_2)\|e[t_2]\rangle = \zeta^{a_2}_{ee}$, $\langle b_2[t_2]\|\vec{s}\vec{u}(e)\|e[t_2]\rangle = \zeta^{e}_{b_2e}$, (notations in square brackets refer to the parentheses from the tetrahedral e and t_2 species).

Symmetry notations for the real $3d$ orbitals in D_{2d} are written on the left-hand side along with conventions for the e-components given in the ADF code. For T_d symmetry, one has to take

$$\langle e\|\vec{s}\vec{u}(t_1)\|t_2\rangle = \zeta^{t_1}_{et_2} = \zeta^{e}_{a_1e} = \zeta^{e}_{b_1e} = \zeta^{a_2}_{b_1b_2}$$

$$\langle t_2\|\vec{s}\vec{u}(t_1)\|t_2\rangle = \zeta^{a_2}_{ee} = \zeta^{e}_{b_2e}.$$

	$\zeta^+(d^+_{xy})$	$\eta^+(d^+_{xz})$	$\xi^+(d^+_{yz})$	$\varepsilon^+(d^+_{x^2-y^2})$	$\theta^+(d^+_{z^2})$	$\zeta^-(d^-_{xy})$	$\eta^-(d^-_{xz})$	$\xi^-(d^-_{yz})$	$\varepsilon^-(d^-_{x^2-y^2})$	$\theta^-(d^-_{z^2})$
$b_2^+\zeta^+(d^+_{xy})$				$i\zeta^{a_2}_{b_1b_2}$			$\frac{-i}{2}\zeta^{e}_{b_2e}$	$\frac{1}{2}\zeta^{e}_{b_2e}$		
$e:2^+\eta^+(d^+_{xz})$			$\frac{-i}{2}\zeta^{a_2}_{ee}$			$\frac{i}{2}\zeta^{e}_{b_2e}$			$\frac{-i}{2}\zeta^{e}_{b_1e}$	$\frac{\sqrt{3}}{2}\zeta^{e}_{a_1e}$
$e:1^+\xi^+(d^+_{yz})$		$\frac{i}{2}\zeta^{a_2}_{ee}$				$\frac{-1}{2}\zeta^{e}_{b_2e}$			$\frac{-i}{2}\zeta^{e}_{b_1e}$	$-\frac{\sqrt{3}}{2}i\zeta^{e}_{a_1e}$
$b_1^+\varepsilon^+(d^+_{x^2-y^2})$	$-i\zeta^{a_2}_{b_1b_2}$						$\frac{1}{2}\zeta^{e}_{b_1e}$	$\frac{i}{2}\zeta^{e}_{b_1e}$		
$a_1^+\theta^+(d^+_{z^2})$							$-\frac{\sqrt{3}}{2}\zeta^{e}_{a_1e}$	$\frac{\sqrt{3}}{2}i\zeta^{e}_{a_1e}$		
$b_2^-\zeta^-(d^-_{xy})$		$\frac{-i}{2}\zeta^{e}_{b_2e}$	$\frac{-1}{2}\zeta^{e}_{b_2e}$						$-i\zeta^{a_2}_{b_1b_2}$	
$e:2^-\eta^-(d^-_{xz})$	$\frac{i}{2}\zeta^{e}_{b_2e}$			$\frac{1}{2}\zeta^{e}_{b_1e}$	$-\frac{\sqrt{3}}{2}\zeta^{e}_{a_1e}$			$\frac{i}{2}\zeta^{a_2}_{ee}$		
$e:1^-\xi^-(d^-_{yz})$	$\frac{1}{2}\zeta^{e}_{b_2e}$			$-\frac{i}{2}\zeta^{e}_{b_1e}$	$-\frac{\sqrt{3}}{2}i\zeta^{e}_{a_1e}$		$-\frac{i}{2}\zeta^{a_2}_{ee}$			
$b_1^-\varepsilon^-(d^-_{x^2-y^2})$		$-\frac{1}{2}\zeta^{e}_{b_1e}$	$\frac{i}{2}\zeta^{e}_{b_1e}$			$i\zeta^{a_2}_{b_1b_2}$				
$a_1^-\theta^-(d^-_{z^2})$		$\frac{\sqrt{3}}{2}\zeta^{e}_{a_1e}$	$\frac{\sqrt{3}}{2}i\zeta^{e}_{a_1e}$							

Appendix 2: DFT Treatment of Jahn–Teller Activity in the Case of Mixing of Electronic States

The Hamiltonian of the ${}^3T \otimes e$ Jahn–Teller problem in a linear approximation

$$H = (1/2)K_e(Q_\theta^2 + Q_\varepsilon^2)\cdot I + V_eQ_\theta \cdot C_\theta + V_eQ_\varepsilon \cdot C_\varepsilon, \tag{A2.1}$$

where I is the identity matrix and C_θ and C_ε are 3×3 matrices taken on the basis of the T_1 α, β, and γ wavefunctions:

$$C_\theta = \begin{bmatrix} \frac{1}{2} & 0 & 0 \\ 0 & \frac{1}{2} & 0 \\ 0 & 0 & -1 \end{bmatrix}; \qquad C_\varepsilon = \begin{bmatrix} -\frac{\sqrt{3}}{2} & 0 & 0 \\ 0 & \frac{\sqrt{3}}{2} & 0 \\ 0 & 0 & 0 \end{bmatrix}. \tag{A2.2}$$

TABLE A2.1

Mixing coefficients c_1 and c_2 of $^3T_1(e^4t_2^4)$ and $^3T_1(e^3t_2^5)$ in the $^3T_1$ ground-state function, DFT optimized angles $\delta\theta° = \theta° - \theta_{T_d}$ and E_{JT} values for $^3T_1(e^3t_2^5)$, force field constants, and vibronic coupling parameters K''_e, V''_e, K'_e, V'_e, and K_e, V_e of $^3T_1(e^3t_2^5)$, $^3T_1(e^4t_2^4)$ and the $^3T_1$ ground state (taking mixing into account) for NiX_4^{2-} (X=F$^-$, Cl$^-$, Br$^-$, I$^-$). *

Species	c_1	c_2	$\delta\theta$	E_{JT}	K''_e	V''_e	K'_e	V'_e	K_e	V_e
NiF_4^{2-}	−0.944	0.330	34.4	−8655	12792	14883	22234	−6049	21206	−3770
$NiCl_4^{2-}$	−0.953	0.303	15.5	−2599	13721	8447	10549	−2334	10840	−1344
$NiBr_4^{2-}$	−0.955	0.297	13.3	−1907	11948	6752	7686	−1747	8064	−998
NiI_4^{2-}	−0.956	0.292	10.1	−1247	11517	5360	2122	−453	2921	43

* For values of $\delta\theta°$ and E_{JT} for the $^3T_1(e^4t_2^4)$ DFT optimized single determinant energy, see the entries in square brackets in Table I. K_e, V_e, and E_{JT} parameters have been expressed in cm^{-1}/Å^2, cm^{-1}/Å, and cm^{-1}, respectively, $\delta\theta$ in °.

Q_θ and Q_ε are the higher and lower symmetric components of the e-vibration, which distorts the tetrahedron into D_{2d} and D_2 geometries, respectively. If we restrict ourselves to distortions of the Q_θ type and define Q_θ as being positive for tetragonal compression, Eq. (A2.1) simplifies to Eq. (A2.3) for the nondegenerate ground state ($^3A_2$ in D_{2d}) and to Eq. (A2.4) for the degenerate higher energy state (^3E). Minimization of Eq. (A2.3)

$$^3A_2 : E(T_1, \gamma) = (1/2)\,K_eQ_\theta^2 - V_eQ_\theta \tag{A2.3}$$

$$^3E : E(T_1, \alpha, \beta) = (1/2)\,K_eQ_\theta^2 + (1/2)V_eQ_\theta \tag{A2.4}$$

with respect to Q_θ yields the equilibrium geometry Q_θ° and the Jahn–Teller stabilization energy E_{JT}:

$$Q_\theta^\circ = V_e/K_e \tag{A2.5}$$

$$E_{JT} = -(1/2)V_e^2/K_e. \tag{A2.6}$$

If we take θ (in °) to be the angle between the S_4 axis and the TM–ligand bond (for the tetrahedron we have $\theta_{T_d} = 54.73°$) Q_θ° (in radians · Å) can be calculated from Eq. (A2.7):

$$Q_\theta = R(\theta° - \theta_{T_d})(\pi/180). \tag{A2.7}$$

In tetrahedral NiX_4^{2-} complexes, the $^3T_1$ wave function $\psi(^3T_1)$ is given by:

$$\psi(^3T_1) = c_1 \quad \psi(^3T_1, e^4t_2^4) + c_2 \quad \psi(^3T_1, e^3t_2^5), \tag{A2.8}$$

where c_1 and c_2 (Table A2.1) are given by the ground state eigenvector diagonalizing the matrix

$$\begin{matrix} & ^3T_1(e^4t_2^4) & ^3T_1(e^3t_2^5) \end{matrix}$$

$$\begin{bmatrix} 0 & 6B \\ 6B & 9B + 10\ \mathrm{Dq} \end{bmatrix}. \tag{A2.9}$$

The $^3T_1(e^4t_2^4)$ and $^3T_1(e^3t_2^5)$ states before the mixing are described by single determinants and their equilibrium geometries (elongation, Table I and compression, Table A2.1) and energies E_{JT} can be calculated from separate DFT geometry optimizations to yield corresponding parameters K_e and V_e [via Eqs. (A2.5) and (A2.6)]. Let us denote these parameters by K'_e, V'_e, and K''_e, V''_e, respectively. Then K_e and V_e after mixing are given by:

$$K_e = c_1^2K'_e + c_2^2K''_e \tag{A2.10}$$

$$V_e = c_1^2V'_e + c_2^2V''_e. \tag{A2.11}$$

Substitution into Eq. (A2.5) yields the equilibrium distortion Q_θ° and using Eq. (A2.7) we get the equilibrium angle $\theta°$. This is given in Table I. Parameter values summarizing the logical steps of this procedure are listed in Table A2.1.